Hindawi
Adsorption Science & Technology
Volume 2022, Article ID 5945169, 12 pages
https://doi.org/10.1155/2022/5945169

Research Article

Synthesis of CeO_2-Fe_2O_3 Mixed Oxides for Low-Temperature Carbon Monoxide Oxidation

Chuc Ngoc Pham,[1] Quyen Van Trinh,[2] Dang Van Thai,[3,4] Nhiem Ngoc Dao,[1,5] Bac Quang Nguyen,[1,5] Dung Trung Doan,[1] Hung Bao Le,[5,6] Vinh Van Nguyen,[6] Lim Thi Duong,[7] and Lam Dai Tran[8]

[1]*Institute of Materials Science, Vietnam Academy of Science and Technology, 18 Hoang Quoc Viet, Hanoi 10000, Cau Giay, Vietnam*
[2]*VNU - Hanoi School of Business and Management (VNU- HSB), 144 Xuan Thuy, Cau Giay, Hanoi 100000, Vietnam*
[3]*Institute of Theoretical and Applied Research, Duy Tan University, Hanoi 100000, Vietnam*
[4]*Faculty of Environmental and Chemical Engineering, Duy Tan University, Da Nang 550000, Vietnam*
[5]*Graduate University of Science and Technology, Vietnam Academy of Science and Technology, 18 Hoang Quoc Viet, Cau Giay, Hanoi 10000, Vietnam*
[6]*Vietnam-Russian Tropical Centre, Cau Giay, Hanoi 10000, Vietnam*
[7]*Institute of Geography, Vietnam Academy of Science and Technology, 18 Hoang Quoc Viet, Hanoi 10000, Cau Giay, Vietnam*
[8]*Institute for Tropical Technology, Vietnam Academy of Science and Technology, 18 Hoang Quoc Viet, Cau Giay, Hanoi 10000, Vietnam*

Correspondence should be addressed to Dang Van Thai; dangvanthai2@duytan.edu.vn

Received 7 October 2021; Revised 28 January 2022; Accepted 7 February 2022; Published 10 March 2022

Academic Editor: Ming Hua

In this study, the CeO_2-Fe_2O_3 mixed oxide catalysts have been prepared by combustion method using gel-created tartaric acid. The ability of effective carbon monoxide (CO) oxidation to carbon dioxide (CO_2) by CeO_2-Fe_2O_3 catalyst under low-temperature conditions was also demonstrated. The calcined CeO_2-Fe_2O_3 material has a porous honeycomb structure and good gaseous absorption-desorption ability. The solid solution of CeO_2-Fe_2O_3 mixed oxides was formed by the substitution of Fe^{+3} ions at some Ce^{4+} ion sites within the CeO_2 crystal lattice. The results also showed that the calcination temperature and the molar ratio of Ce^{3+} ions to Fe^{3+} ions (CF) affected the formation of the structural phase and the catalytic efficiency. The catalytic properties of the CeO_2-Fe_2O_3 mixed oxide were good at the CF ratio of 1 : 1, the average crystal size was near 70 nm, and the specific surface area was about 20.22 $m^2.g^{-1}$. The full conversion of CO into CO_2 has been accomplished at a relatively low temperature of 270 °C under insufficient O_2 conditions.

1. Introduction

Every year, the world emits a large amount of CO gas from thermal power plants, metallurgical plants, vehicles, wood burning, and waste burning. According to research in several developmental countries, thousands of people are died each year due to CO gas poisoning [1, 2]. The easy cause of CO gas poisoning is because its colorless, odorless, and nontoxic properties are difficult to recognize. *CO gas* is the incomplete oxidation product of carbon compounds at low temperatures and O_2 deficiency [3–5]. Under suitable conditions, CO exhibits strong reducing properties for medium metal oxides, so it has been studied and used in the metallurgical industry early [6]. Because of its possible toxic property to humans, the study and treatment of CO gas together with its secondary CO_2 product are very important. In some

technical and industrial fields, CO_2 has begun to be captured and applied to reduce the greenhouse effect [7]. There are two popular methods for CO treatment as follows: adsorbing to capture CO gas [8–10] or converting CO to CO_2 by metal oxide catalysts [11].

Nowadays, CeO_2 is one of the important metal oxides in gas conversion catalysis. Cerium (Ce) belongs to the rare earth family and orders the second in the lanthanide series. Ce reserves account for a small proportion of the earth's crust, so exploitation is difficult and expensive. Ce has the electron configuration $[Xe]4f^15d^16s^2$, which it can exist in the oxidation states Ce^{+3} ($[Xe]4f^15d6s$) and Ce^{+4} ([Xe] 4f5d6s). Thus, CeO_2 and Ce_2O_3 are the compounds of Ce with oxygen, and CeO_2 is more stable due to the electron configuration of Ce^{+4} ([Xe]4f5d6s) being similar to that of the inert xenon gas [12]. The flexible conversion of the two Ce^{4+} and Ce^{3+} states through the electron donor mechanisms on the surface of CeO_2 makes it widely used in catalytic reactions such as wastewater treatment [13–16], water-gas phase transition [17], and gas conversion [18–21]. CeO_2 oxides can be prepared by hydrothermal method [21, 22], coprecipitation [23–25], sol-gel [19, 26], impregnation [27], and combustion [18]. The choice of the fabrication method decides the crystal structure, morphology, and physicochemical properties of CeO_2, leading to affect the CO conversion ability of the catalyst [21, 22, 28]. The surface of the fabricated CeO_2 crystals is often imperfect due to lattice defect, vacuous O^{2-} ion (denoted V_O) sites, and unsaturated bonds leading to the existence of Ce^{3+} and Ce^{4+} states [20, 29]. The ratio between the number of Ce^{3+} ions to Ce^{4+} ions (Ce^{3+}/Ce^{4+}) is related to the number of V_O vacancies on the CeO_2 crystal surface, so it determines the oxygen storage capability and oxygen lease capability [25]. When the Ce^{3+}/Ce^{4+} ratio is large, the number of V_O vacancies on the surface is also large [30]. Besides, the number of V_O also depends on the crystal morphology, and it decreases gradually with nanorods > cubes nanoscale > nanopolyhedra [29]. The density functional theory (DFT) calculations show that for low-index faces, the energy to release an O^{2-} ion from the lattice to create a V_O vacancy of (111) face is the largest in comparison with the (110) and (100) face, so the number of V_O on the faces decreases in the order (110) > (100) > (111) [29]. In addition, CeO_2 is a direct bandgap semiconductor with bandgap energies of 2.56 eV for the bulk sample and 3.23 eV for the nanoscale, corresponding to the absorption transition energy 2p (O^{2-}) →4f (Ce^{4+}) [26, 30]. When an O^{2-} ion on the crystal surface gets an excitation agent to promote the electron transition 2p → 4f, it will separate from the crystal lattice leaving a V_O vacancy in company with the oxidation state transformation $Ce^{+4}(4f^0) \rightarrow Ce^{+3}(4f^1)$ [11]. V_O vacancies are capable of adsorbing CO or O_2 molecules at these positions, so they play an important role in catalytic reactions. An O_2 molecule can be captured by a V_O vacancy to form an O^{2-} lattice ion [31]. The combination reactions of CO molecules with the absorbed O_2 molecules on the surface of the oxide catalyst are occurred by the Langmuir-Hinshelwood (L-H) mechanism or with the O^{2-} ions of the lattice by the Mars-van Krevelen (M-K) mechanism [29]. The CeO_2 oxide catalyst material becomes thermal stable, has a fast catalytic rate, and has a low catalytic temperature when combined with some rare metals such as Pt [32], Pd [33], Au [34], and Ag [35]. However, a current trend uses the low-cost transition metal iron (Fe) element to make Fe_2O_3-CeO_2 mixed oxides. In nature, iron exists in both Fe^{2+} and Fe^{3+} oxidation states. The radius of Fe^{3+} ion (0.64 Å) is smaller than that of Ce^{4+} ion (1.01 Å), so the substitution of Fe^{3+} ions in some Ce^{4+} ion positions can shrink the CeO_2 crystal lattice, the 2θ diffraction angle positions of the (111) face is shifted towards the larger angle, and the formed possibility of V_O vacancies is also increased [36]. The optical absorption transition properties of Fe_2O_3 oxide include the direct charge transition $O^{2-}(2p) \rightarrow Fe^{3+}(3d)$ in the ultraviolet region and the indirect charge transition between $Fe^{3+}(3d)$ states in the visible region [37]. The conversion ability between Fe^{3+} and Fe^{2+} ions become even more flexible in Fe_2O_3-CeO_2 composition, which is demonstrated through photochemical reactions treating organic pigments [15]. The O^{2-} ions of the Fe-O-Ce bonds react better with CO than that of the Ce-O-Ce bonds [38], even so than those of Fe-O-Fe bonds. The energy separates an O^{2-} atom from the surface to create a V_O vacancy of about 3.04 eV [39]. The redox potential of the Fe^{+3}/Fe^{+2} pair (0.71 eV) is smaller than that of the Ce^{+4}/Ce^{+3} pair (1.61 eV), which facilitates the electron donor-acceptor processes and the oxidation state transformation of Ce^{+4}/Ce^{+3} and Fe^{+3}/Fe^{+2} pairs [20]. Other studies show that the combination of Ce and Fe elements forms CeO_2-Fe_2O_3 mixed oxide, which can reduce the reactive catalytic temperature of 50% (T_{50}) and 100% (T_{100}) CO conversion in comparison with single oxide catalysts of CeO_2 and Fe_2O_3, depending on the fabrication method [31, 40, 41].

From the above-mentioned characteristics, it shows that the CeO_2-Fe_2O_3 mixed oxide material has many advantageous photochemical properties that need further studying and applying for life. This study was carried out with the purpose of making CeO_2-Fe_2O_3 mixed oxide materials from popular Fe metal, reducing the content of rare earth Ce and the reactive catalytic temperature of complete CO conversion to CO_2 while applying to treat the exhaust gas in simple incinerators.

2. Chemicals and Experiments

2.1. Preparation of Mixed Oxide Catalysts. High-purity chemicals were used as $Fe(NO_3)_3{\cdot}6H_2O$ (99.98%), $Ce(NO_3)_3{\cdot}6H_2O$ (99.98%), and tartaric acid (TA) (99.98%). TA was dissolved with twice distilled water at 80 °C to get A solution. The above nitrate salts were also dissolved to give B solution such that the molar ratio of CF mixture to TA solution always was 1 : 3. A regulator matter was utilized to keep the pH of the solution equal to 2. The B solution was slowly added to the A solution, stirred, and heated at 80 °C for 2 h to obtain a pale-yellow homogeneous gel solution. The gel was then dried at 100 °C for 4 h to obtain a porous shape sample. The obtained sample was analyzed by TGA to investigate the phase transition of the sample in accordance with the calcination temperature. The samples calcined in turn at 450, 550, 650, 750, 850, and 950 °C for 2 h to obtain mixed

oxides which denote as CF450, CF550, CF650, CF750, CF850, and CF950. To investigate the influence of the CF molar ratio on the structural phase formation of mixed oxides, the weight of the nitrate salts in the B solution was calculated so that the CF molar ratio of the obtained gels is in turn 9 : 1; 3 : 1; 1 : 1; 1 : 3, and 1 : 9. These gels, calcined at 650 °C for 2 h, received the mixed oxides of CF91, CF31, CF11, CF13, and CF19, respectively.

2.2. Analytics

2.2.1. Differential Thermal Analysis and Thermogravimetric Analysis. Differential thermal analysis (DTA) and thermogravimetric analysis (TGA) were performed on a Labsys Evo 1600 system. Samples were measured in air, heating rate 10 °C.min^{-1}.

2.2.2. X-Ray Diffraction Analysis. X-ray diffraction (XRD) measurements of the studied samples were performed on a Siemens D5000 X-meter.

2.2.3. Scanning Electron Microscopy Image. The surface morphology of the materials was recorded by scanning electron microscopy (SEM). Samples were measured on a Hitachi S-4800 instrument operating at 10 kV with a magnification of 80000-100000 times.

2.2.4. Determine the Specific Surface Area. The sample surface area was determined by the Brunauer-Emmett-Teller (BET) method on the Autosorb IQ Station measuring system. BET equation: $P/[V(P_o - P)] = 1/V_m C + [(C-1)/V_m C].P/P_o$, where P is the equilibrium pressure, P_o is the saturated vapor pressure of the adsorbed gas at experimental temperature, V is the volume of the adsorbed gas at pressure P, and V_m is the saturated gas volume of monolayer adsorption per 1 gram of adsorbent, and C is the BET constant. The specific surface area BET (S_{BET}) of the material is calculated according to the equation: $S_{BET} = (V_m/M).N\,A_m\,d$, where d is the density, M is the molar mass of the adsorbent, respectively, N is the Avogadro number ($N = 6.023 \times 10^{23}$ molecules.mol^{-1}), and A_m is the cross-sectional area of 1 molecule occupied on the surface adsorbent.

2.2.5. Fourier Transform Infrared Spectra. The Fourier transform infrared (FTIR) spectra of the samples were recorded in the range of wavenumbers from 400 cm^{-1} to 4000 cm^{-1} on the Impact 410 spectrometer.

2.2.6. Determination of CO Conversion. The TPSR temperature surface response program was conducted with a Siemens temperature controller. The CO conversion of the catalytic material performing on the microcurrent device was calculated by the following formula: $H\,(\%) = (C_f/C_o).100\%$, where H is the CO (%) conversion and C_o and C_f are the CO concentrations before and after catalysis, respectively.

3. Results and Discussions

3.1. DTA and TGA Spectra of CeO_2-Fe_2O_3 Mixed Oxides. The DTA and TGA spectra of the gel sample with the CF/TA ratio of 1 : 3 presented in Figure 1. The DTA curve showed the temperature increased from 100 °C to 250 °C. The sample weight decreased by 38.89%, with an endothermic peak at 217 °C. This reduction may be due to the physical evaporation of the adsorbed water on the gel surface [42, 43]. In the temperature range from 250 °C to 550 °C, the sample weight decreased by 34.83% on the TGA curve corresponding to the exothermic peak of 328 °C on the DTA curve, which was caused by the pyrolysis processes of the nitrate salts released O_2 and NO_2 gas; the combustion process of the TA released CO_2 gas and H_2O according to the following reactions (1), (2), and (3) [43, 44]:

$2C_4H_6O_6 + 5O_2 \rightarrow 8CO_2\uparrow + 6H_2O$ (1)

$4Fe(NO_3)_3 \rightarrow 2Fe_2O_3 + 12NO_2\uparrow + 3O_2\uparrow$ (2)

$2Ce(NO_3)_3 \rightarrow 2CeO_2 + 6NO_2\uparrow + O_2\uparrow$ (3)

or $4Fe(NO_3)_3 + 2Ce(NO_3)_3 + 2C_4H_6O_6 + O_2 \rightarrow 2(Fe_2O_3\text{-}CeO_2) + 18NO_2\uparrow + 8CO_2\uparrow + 6H_2O$ (4)

When the temperature increased from 550 °C to 900 °C, the sample weight was almost unchanged, showing that the Fe_2O_3-CeO_2 mixed oxide was formed and stable.

3.2. FTIR Spectra of CeO_2-Fe_2O_3 Mixed Oxides. The appearance of vibrations characterized to the bonds of CeO_2-Fe_2O_3 mixed oxide determined via the FTIR spectra. In Figure 2, the FTIR spectra of all samples in the broad absorption range from 3000 cm^{-1} to 3500 cm^{-1} appeared a peak at about 3378 cm^{-1} characterized by the stretching vibration of the O-H group because of the physically adsorbed water; however, this peak intensity decreased gradually as the calcination temperature of samples increased. A peak at about 2337 cm^{-1} characterized the stretching vibration of adsorbed CO_2 molecules from the air for CF450, CF550, and CF650 samples, and this peak was completely suppressed for CF750 and CF850 samples. The peaks at 1630, 1380, and 1121 cm^{-1} represented the C=O and C-O stretching vibrations of the -COO- group [42, 43]. At the high calcination temperature, the process of CO_2 separation occurred, so the absorption intensity of the band related to -COO- decreased and expanded into a large halo as on the CF850 sample. It is noteworthy that the appearance of the peak at 529 cm^{-1} with strong absorption intensity for samples calcined at 850 °C was typical for Fe-O vibrations, the peaks of 643 and 443 cm^{-1} were characteristic of Ce-O vibrations [42, 43, 45], and the above peaks appeared clear for the CF650 sample. This also shows that the characteristic phases of the CeO_2-Fe_2O_3 mixed oxide were soon formed, and it was also consistent with the result of the TGA-DTA analysis.

3.3. The Role of Calcination Temperature and Metal Ion Molar Ratio in the Structural Phase Formation of CeO_2-Fe_2O_3 Mixed Oxides

3.3.1. The Role of Calcination Temperature. The thermogravimetric analysis shows that the suitable calcination

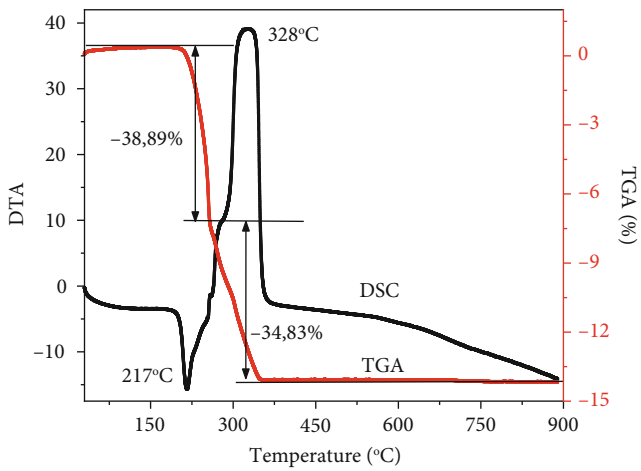

Figure 1: TGA and DTA spectra of the gel sample with the CF/TA ratio of 1 : 3.

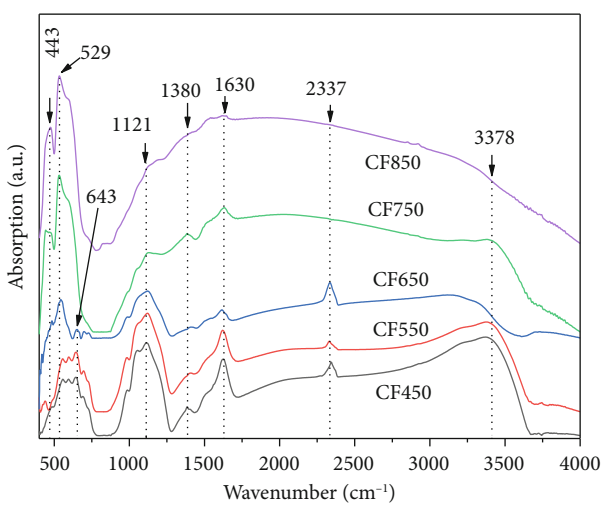

Figure 2: FTIR spectra of gel samples with the CF/TA ratio of 1 : 3 calcined at different temperatures for 2 h.

temperature range was from 450 to 900 °C. Figure 3 presents the XRD pattern of the CeO_2-Fe_2O_3 mixed oxides calcined at 450, 550, 650, 750, 850, and 900 °C for 2 h. At 450 °C and 550 °C, the XRD pattern of CF450 and CF550 only appeared the (111), (200), and (220) faces corresponding to the 2θ diffraction angles at 28.96°, 33.11°, and 47.47° (JCPDS No. 34-0394), in which the (111) face had the greatest intensity. These faces characterized the face-centered cubic structure of CeO_2 in mixed oxides [36]. Meanwhile, at these calcination temperatures, there were almost no faces that characterized the structural phase of Fe_2O_3. This may be because the samples had not reached good crystallinity, and the crystal structure was not complete. At 650 °C, the reflection faces characterizing the structural phase of Fe_2O_3 also occurred clearly and intertwined with those of CeO_2 as the represented spectrum of the CF650 sample in Figure 3(b). The (311), (222), (400), (331), (420), (422), and (511) faces corresponded to 2θ diffraction angles of 56.32°, 59.02°, 69.42°, 76.66°, 79.92°, 88.39°, and 95.04° belonged to the CeO_2 crystal structure, but the (012), (110), (024), and (116) faces assigned to 2θ angles of 24.92°, 35.64°, 49.46°, and 54.02°, respectively, representing the hexagonal structure phase of Fe_2O_3 (JCPDS No. 33-0664) [14, 19, 27].

The diffraction intensity on all faces became narrower and stronger as the calcination temperature increased. This meant that the samples had better crystallinity, a complete crystal structure, and larger crystal sizes [46]. However, when the samples calcined to 750 °C and 850 °C, a separating tendency of mixed oxide phase into two single oxide phases of CeO_2 and Fe_2O_3 was happened because of these more thermal stable oxides. Based on the XRD pattern and Brass' formula, it is able to determine the *a* lattice constant via the (111) face of all the CeO_2-Fe_2O_3 mixed oxides, as seen in Table 1.

The results showed that there was a slight increase of the *a* lattice constant from 5.3385 to 5.3530 Å, corresponding to a slight decrease of the 2θ diffraction angle from 28.96 to 28.89 Å. The increase of the *a* lattice constant together with the left shift of the 2θ angle indicated that the calcination sample at 450°C had formed in a solution of CeO_2-Fe_2O_3 mixed oxide [23]. It is explained that the Fe^{3+}(0.64 Å) ion radius is smaller than the Ce^{4+} (1.01 Å) ion radius, so when the Ce^{4+} ions are replaced by Fe^{3+} ions at some CeO_2 lattice sites, these substitutions cause the shrink of the crystal lattice [36]. In contrast, the partial separation of the CeO_2 phase widened the crystal lattice and shifted the 2θ angle position of the (111) face towards a smaller angle as illustrated by CF450, CF650, and CF850 patterns in the small inset of Figure 3(b). Thus, it can be seen that the change in calcination temperature affected the formation of mixed oxide solution. At 650°C, the crystal was complete with the appearance of both CeO_2 and Fe_2O_3 phases. When the calcination temperature of the sample increased, the mixed oxides had good crystallization and tended to the segregation of single oxide phases.

3.3.2. The Role of Metal Ion Molar Ratio. XRD pattern of CeO_2-Fe_2O_3 mixed oxides with different CF molar ratios calcined at 650 °C for 2 h, as seen in Figure 4. When the molar quantity of Ce^{3+} ions was more than that of Fe^{3+} ions (CF91 and CF31 samples), the XRD pattern manifested the (111), (200), (220), (311), (222), (400), (331), (422), and (511) faces corresponded to the 2θ diffraction angles of 28.82°, 33.11°, 47.47°, 56.32°, 59.07°, 69.41°, 76.64°, 79.91°, 88.39°, and 95.04° and characterized the crystalline structure phase of CeO_2 (for CF91 and CF31 samples in Figure 4(a)) [14, 19, 27].

This may be because with the calcination condition to 650 °C, and the used Fe^{3+} ion content was smaller in comparison with the Ce^{4+} ion content, so Fe^{3+} ions were dissolved in the crystal lattice of CeO_2 oxide [23]. When the molar quantity of Ce^{3+} ion and Fe^{3+} ions was equal, the characteristic faces of the Fe_2O_3 phase appeared and interwove with those of CeO_2, and the XRD pattern of CF11 was presented again in Figure 4(b). The presence of the typical (110) face of Fe_2O_3 shows that the mixed oxide has

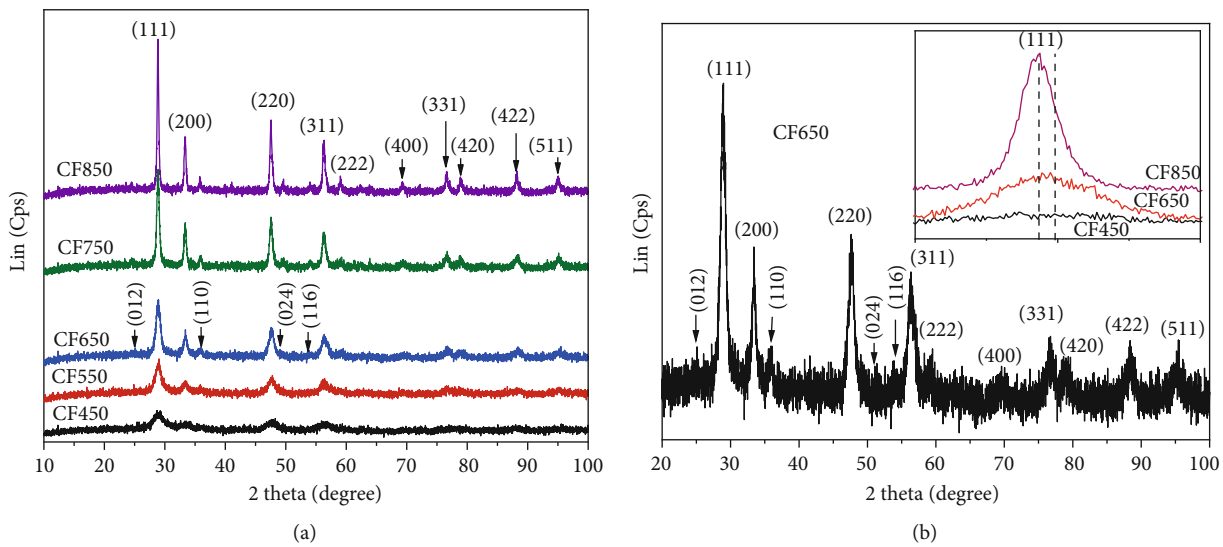

Figure 3: XRD pattern of CeO_2-Fe_2O_3 mixed oxides. Samples with the CF molar ratio of 1 : 1 calcined at different temperatures for 2 h (a) and CF650 sample was redrawn (b).

Table 1: 2θ diffraction angle and a lattice constant of CeO_2-Fe_2O_3 mixed oxides calcined at different temperatures for 2 h.

Sample	CF450	CF550	CF650	CF750	CF850
Diffraction angle 2θ (degree)	28.96	28.94	28.92	28.89	28.88
Lattice constant a (Å)	5.3385	5.3422	5.3458	5.3512	5.3530

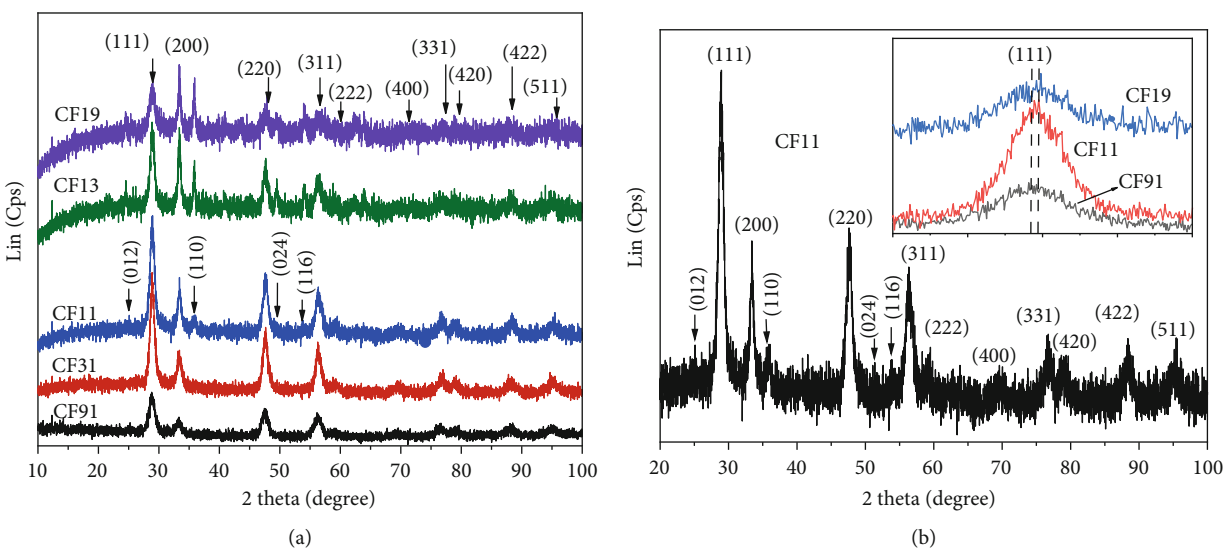

Figure 4: XRD patterns of CeO_2-Fe_2O_3 mixed oxides. Samples with different CF molar ratios calcined at 650 °C for 2 h (a) and CF11 sample was redrawn (b).

separated into phases [47]. When the molar quantity of Ce^{3+} ions was smaller than those of Fe^{3+} ions (for CF13 and CF19 samples), the diffraction intensity on the (110) face became more narrow and stronger. This phenomenon was known that the molar quantity of Fe^{3+} ions in mixed oxides was high, which led to the split gradually mixed oxides into two individual oxide phases of CeO_2 and Fe_2O_3 [23]. The a lattice constants of CeO_2 were calculated from the (111) face in Table 2. As a result, there was a slight decrease of a lattice constant from 5.3639 Å to 5.3385 Å, while the 2θ diffraction angle of the (111) face shifted towards the greater diffraction angle from 28.82° to 28.98°, respectively. This

Table 2: 2θ diffraction angle and a lattice constant of CeO_2-Fe_2O_3 mixed oxides with different CF molar ratios calcined at 650 °C for 2 h.

Sample	CF91	CF31	CF11	CF13	CF19
Diffraction angle 2θ (degree)	28.82	28.87	28.92	28.94	28.98
Lattice constant a (Å)	5.3639	5.3548	5.3458	5.3421	5.3385

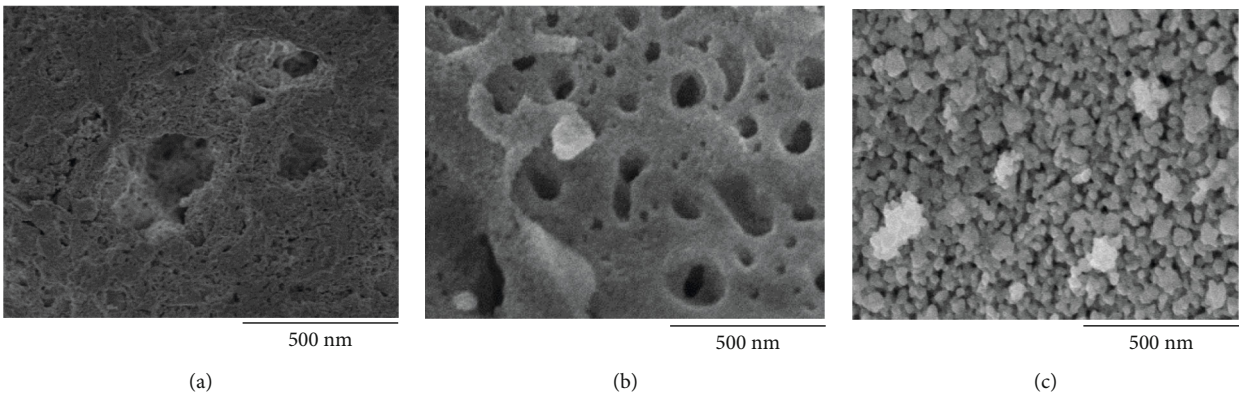

Figure 5: SEM images of CeO_2-Fe_2O_3 mixed oxides with the CF ratio of 1 : 1 calcined at 450 °C (a), 650 °C (b), and 850 °C (c) for 2 h.

shift can observe clearly by CF91, CF11, and CF19, as seen in the small inset in Figure 3(b) [20, 23, 24, 36]. The above results showed that the change in CF molar ratio also affected the formation of the crystal structure phase of the mixed oxides. With a CF molar ratio of 1 : 1, there appeared characteristic reflection faces for the structural phases of CeO_2 and Fe_2O_3. When the molar quantity of Fe^{3+} ions were high, the CeO_2-Fe_2O_3 mixed oxide tended to separate into two oxide phases of CeO_2 and Fe_2O_3.

3.4. Morphology of Fe_2O_3-CeO_2 Mixed Oxides. SEM images of the CeO_2-Fe_2O_3 mixed oxides were shown in Figure 5 with the CF molar ratio of 1 : 1 which were calcined at temperatures of 450 °C, 650 °C, and 850 °C for 2 h. It is observed that the surface of the CF450 sample was porous. This is the characteristic of materials that are prepared by the combustion method using organic compounds to create gels (Figure 5(a)) [48]. For the CF650 sample, the porous property became clear to many honeycomb-like cavities. It can be explained that the molecular structure of TA consists of strongly polar functional groups HOOC(HO)CC(OH) COOH that played the role of stretching and uniformly dispersing Ce^{3+} and Fe^{3+} ions in solution [49]. At 650 °C, the decomposition of the organic component and the pyrolysis of nitrate salts led to a decrease in volume and mass, creating a system of space-connected microcapillary tubes (Figure 5(b)). This created a porous property of mixed oxides as well as the obtained result in other reports [50]. The average crystal size of the oxide was determined to be about 70 nm. For the CF850 sample, the crystals tended to break the spatial porous block into discrete nanosized particles (Figure 5(c)) [42].

From the dependence of $P/[V(P_o - P)]$ on P/P_o in the BET equation, the adsorption-desorption isotherm representing the relation between the adsorbed volume and the relative pressure was shown in Figure 6. The linear shape

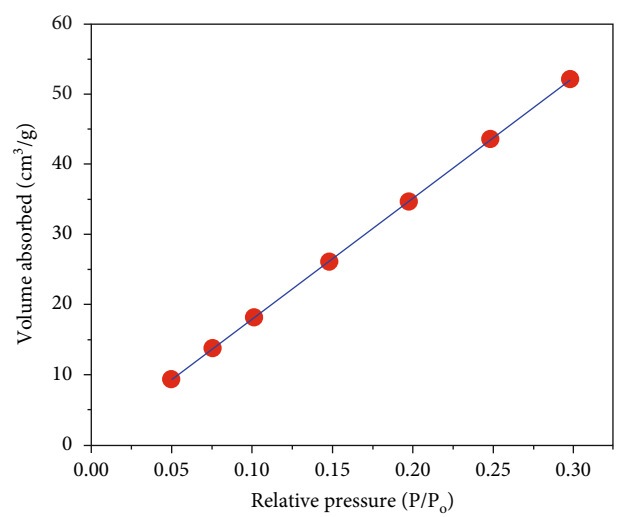

Figure 6: Nitrogen adsorption-desorption isotherms of CeO_2-Fe_2O_3 mixed oxide with the CF molar ratio of 1 : 1 calcined at 650 °C for 2 h.

of the isotherm in the low P/P_o value range indicated that monolayer adsorption occurred on the surface of the porous catalyst, and it is also suitable for the linear region in the range of P/P_o from 0.05 to 0.35 of this material [51]. The specific surface area of the CeO_2-Fe_2O_3 mixed oxide, CF650 sample, was determined at about 20.22 $m^2.g^{-1}$.

3.5. Process of CO Conversion to CO_2. The process of CO oxidation by CeO_2-Fe_2O_3 mixed oxide catalysts and the curves of CO conversion according to temperature is described via Figure 7. Under the catalytic temperature condition below 300 °C and deficient O_2 gas, the activities of CO oxidation took place [6]. The CF91, CF31, CF13, and CF19

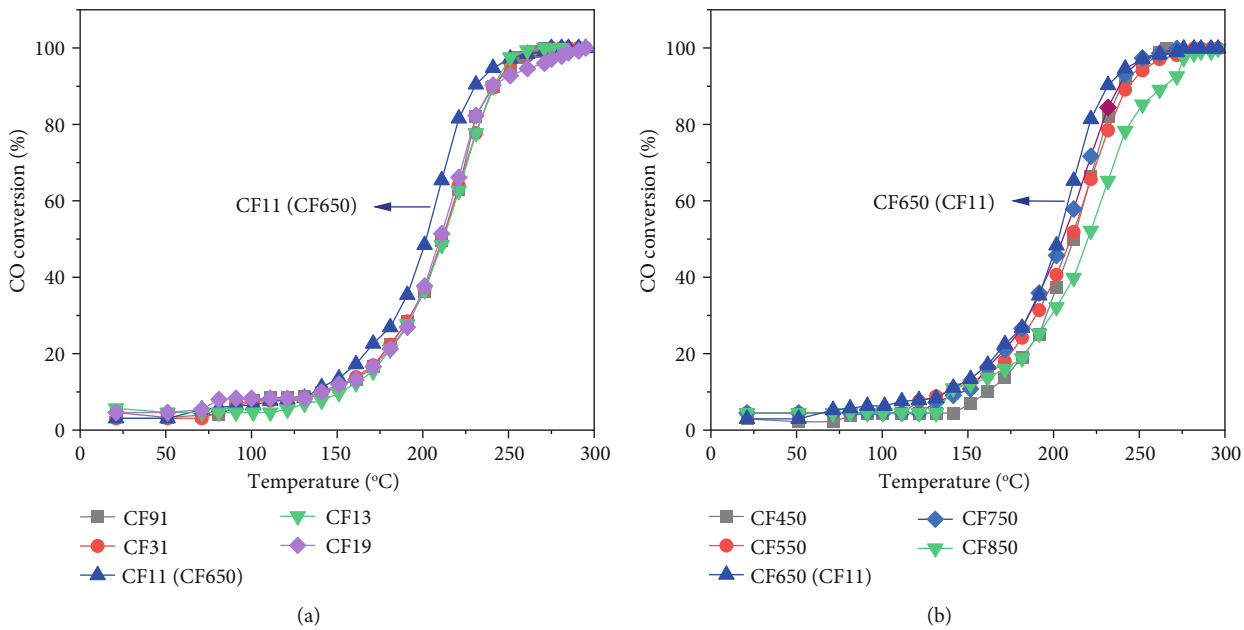

Figure 7: CO conversion of CeO_2-Fe_2O_3 samples according to temperature. Samples with different CF molar ratios calcined at 650 °C for 2 h (a) and samples calcined at different temperatures for 2 h (b).

samples with the different molar quantities of Ce^{3+} and Fe^{3+} ions shown that the CO conversion curves were similar variation, and the ability of CO conversion was lower than that of the CF11 sample (Figure 7(a)). For the CF11 sample (also named as CF11(CF650) or CF650(CF11)), the CO conversion curve was left-skewed, meaning that at the same catalytic temperature, the CO conversion of the CF11 sample was higher and finished earlier than other samples. This can be because the molar quantity of Ce^{3+} and Fe^{3+} ions was the same, the quantity of O^{2-} ions in the -Ce-O-Fe- bonds was more dominant than that in two -Ce-O-Ce and -Fe-O-Fe- bonds of other samples, so the catalytic reactions of CF11 sample also happened better than the others [38]. The CO conversion for all samples can be explained by the following reactions:

$2CO + O_2 \rightarrow 2CO_2\uparrow$ (7)

$2CeO_2 + CO \rightarrow Ce_2O_3 + CO_2\uparrow$ (8)

$3Fe_2O_3 + CO \rightarrow 2Fe_3O_4$ (or $FeO.Fe_2O_3$) $+ CO_2\uparrow$ (9)

$2FeO + 2CeO_2$ (or $2FeO.CeO_2$) $\rightarrow Ce_2O_3 + Fe_2O_3$ (or $Ce_2O_3.Fe_2O_3$) (10)

$2Ce_2O_3 + O_2 \rightarrow 4CeO_2$ (11)

When the catalytic temperature increased from 75 °C to 175 °C, the amount of CO gas was converted about 12%; this may be because a part of CO gas was oxidized by O_2 in (7) [11]. In addition, these reactions can also occur between adsorbed CO and O_2 gases on the surface of the CeO_2-Fe_2O_3 catalyst to emit CO_2 by the J-H mechanism. When the temperature increased from 175 °C to 260 °C, the CO conversion was rapid for all samples but reached the fastest 50% at 211 °C for CF11. The intensification of CO oxidation can be because CO combines with an O^{2-} at the lattice sites in -Ce-O-Fe-, -Ce-O-Ce- and -Fe-O-Fe- bonds to release CO_2 by the M-K mechanism in (8) and (9) [27, 29]. The Fe_3O_4 product was a mixture of two $FeO{\cdot}Fe_2O_3$ oxides, meaning that only a part of Fe^{3+} ions were reduced to Fe^{2+} ions. This low-temperature reaction was also carried out early by another researcher [6].

When the temperature was over 260 °C, the CO conversion process slowed down because it needed the recovery of the CeO_2 oxidizing agent from Ce_2O_3 according to (10) and (11) and then reached 100% at 275 °C faster for the CF11 sample. The recovery here was due to the redox potential of Fe^{+3}/Fe^{+2} (0.711 V) < Ce^{+4}/Ce^{+3} (1.61 V) [20], so a tendency happened the redox process $Ce^{+4} + Fe^{+2} \rightarrow Ce^{+3} + Fe^{+3}$ [23, 52], or this was also the process of transferring an O^{2-} ion from Ce^{4+} ion to a neighboring Fe^{2+} ion, creating the charge balance [38]. The (11) reaction turned Ce^{3+} into initial Ce^{4+}, which was an important agent that helped Fe ion form a closed-loop bridge of oxidation states by the (9) and (10) reactions as follows: $Fe_2O_3 \rightarrow Fe_3O_4 \rightarrow FeO \rightarrow$ -Fe_2O_3. The participation of Fe^{3+} ions in the mixed oxide made the deformation of lattice structure and increased the reaction centers of gases storage and release. Therefore, the conversion of CO to CO_2 became more efficient under low temperatures and O_2 deficiency [4, 5]. It can be seen that thanks to the redox process between Fe^{+2} and Ce^{+4}, the catalyst system was restored to its original properties and was not degraded.

With the same catalytic mechanisms above, among all CeO_2-Fe_2O_3 mixed oxide samples calcined at different temperatures for 2 h, the CO conversion of the CF650 sample was better than all of those (Figure 7(b)). The CF650 curve was also skewed to the left and rapidly reached 100% at 270 °C. It is possible that for the samples CF450 and CF550, the crystallization of the oxides had not been complete, and there were still carbonate components of organic combustion products as analyzed in the TGA-DGT and FTIR spectra, which interfered with the process of CO oxidation. For the CF750 and CF850 samples, the crystal grain size increased, and the surface area decreased, leading to a decrease in the contact and oxidation capacity. Moreover, at high calcination temperature, there was

For the J-H mechanism, a CO molecule reacted with adsorbed an O_2 molecule at Vo vacancy to emit a CO_2 molecule (7):

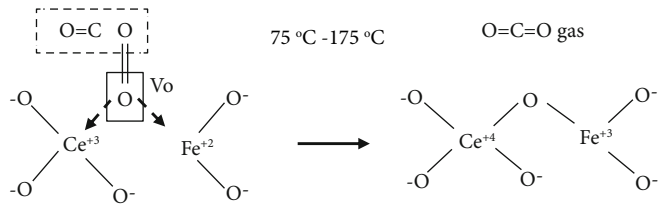

For the M-K mechanism, a CO molecule combined with an O^{2-} ion of the crystal lattice to release a CO_2 molecule and a Vo vacancy (8) and (9):

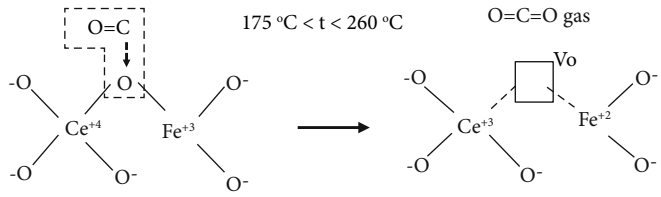

The transformation of Ce^{+4} to Ce^{3+} and Fe^{+2} to Fe^{3+} (10):

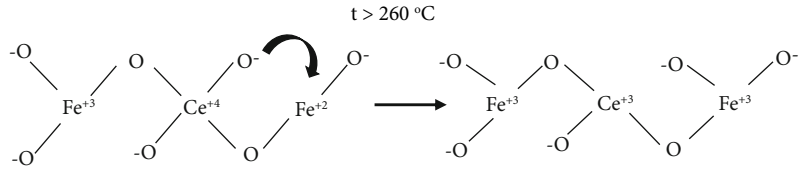

The transformation of Ce^{+4} from Ce^{+3} after an O_2 molecule was captured by a Vo vacancy (11):

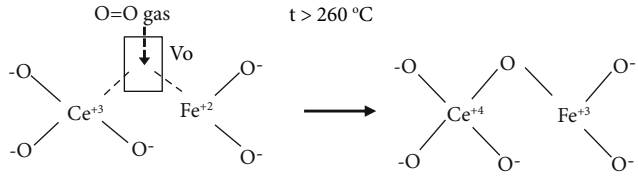

Figure 8: The mechanisms of CO oxidation and the oxidation state conversion of metal ions between Ce^{+4}/Ce^{+3} and Fe^{+3}/Fe^{+2} pairs on the CeO_2-Fe_2O_3 catalyst surface.

a tendency of phase separation into two single oxides as mentioned in the XRD pattern, so their oxidation ability became less than that of mixed oxide catalysts [23]. Thus, the calcination temperature changed the crystallinity and affected the CO catalytic ability of the CeO_2-Fe_2O_3 mixed oxides. From the above arguments, it is able to describe the mechanisms of CO oxidation, capture O_2, and release O^{2-} ions, creating V_O vacancies on the surface of CeO_2 crystal, as shown in Figure 8.

For the J-H mechanism, a CO molecule reacted with adsorbed an O_2 molecule at V_O vacancy to emit a CO_2 molecule (7):

For the M-K mechanism, a CO molecule combined with an O^{2-} ion of the crystal lattice to release a CO_2 molecule and a V_O vacancy (8) and (9).

The transformation of Ce^{+4} to Ce^{+3} and Fe^{+2} to Fe^{+3} was in (10).

The transformation of Ce^{+4} from Ce^{+3} after an O_2 molecule was captured by a V_O vacancy (11):

Table 3: T_{50} and T_{100} temperatures of CeO_2-Fe_2O_3 samples. Samples with different CF molar ratios calcined at 650 °C for 2 h (a) and samples calcined at different temperatures for 2 h (b).

a			b		
Sample	T_{50} (°C)	T_{100} (°C)	Sample	T_{50} (°C)	T_{100} (°C)
CF91	211	275	CF450	211	275
CF31	211	275	CF550	211	280
CF11	200	270	CF650(CF11)	200	270
CF13	211	275	CF750	205	275
CF19	211	295	CF850	221	275

The CO conversion temperatures at T_{50} and T_{100} of all CeO_2-Fe_2O_3 samples are shown in Table 3. It can show that the change of the CF molar ratio and calcination temperature of samples affected the CO conversion of CeO_2-Fe_2O_3 mixed oxide catalysts. The T_{50} and T_{100} temperatures of all

Table 4: T_{50} and T_{100} temperatures of CeO_2, Fe_2O_3, and CeO_2-Fe_2O_3 oxides cited in some other references.

Oxide	Fabricated method	T_{50}	T_M/T_{100} ($T_M < T_{100}$)	Reference
CeO_2	Polyol method	250°C	350°C	[57]
CeO_2	Combustion method	x	~240°C[a]	[58]
CeO_2	Hydrothermal method	216	~230°C	[22]
CeO_2	Combustion method	330°C	~410°C	[52]
CeO_2	Combustion method	~210°C	~260°C[b]	[48]
CeO_2	Co-precipitation method	500 K	700 K	[23]
CeO_2	Microwave and combustion method	362°C	~475°C	[41]
CeO_2	Hydrothermal method	x	~610 K	[55]
CeO_2	Surfactant-templated method	~230°C	~300°C	[46]
CeO_2	Thermal decomposition method	300°C	x	[40]
CeO_2	Solvothermal reaction method	~320°C	~400°C	[56]
Fe_2O_3	Co-precipitation method	620 K	750 K	[23]
Fe_2O_3	Co-precipitation method	290°C	450°C	[54]
Fe_2O_3	Surfactant-assisted method	~220°C	270°C	[53]
CeO_2-Fe_2O_3	Co-precipitation method	500 K	600 K	[23]
CeO_2-Fe_2O_3	Cyclic molecular designed dispersion method	~465 K	548 K	[27]
CeO_2-Fe_2O_3	Co-precipitation method	x	25°C[c]	[25]
CeO_2-Fe_2O_3	Hydrothermal method	166°C	~280°C	[19]
CeO_2-Fe_2O_3	Co-precipitation method	480 K	~575 K	[24]
CeFe10	Thermal decomposition method	203°C	~280°C	[40]
$Ce_xFe_{1-x}O_{2-\delta}$	Co-precipitation method	250°C	~450°C	[31]
$Ce_{0.98}Fe_{0.03}O_2$	Microwave and combustion method	298°C	~375°C	[41]

[a,b,c]The maximum CO conversion catalytic temperatures (T_M) of 30%, 70%, and 96.17%, respectively. x is the reaction catalyst temperature that is unknown or out of measurement scale.

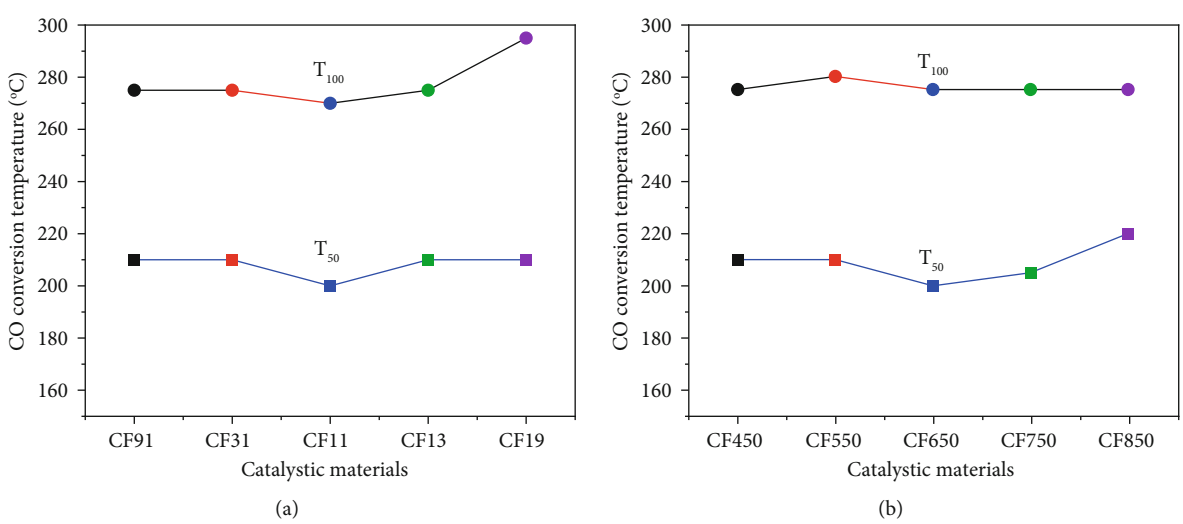

Figure 9: T_{50} and T_{100} temperatures of CeO_2-Fe_2O_3 samples. Samples with different CF molar ratios calcined at 650 °C for 2 h (a) and samples calcined at different temperatures for 2 h (b).

samples are quite low, so it is considered an advantage of this fabrication method. Of all the samples, the T_{50} and T_{100} temperatures of the CF11 (CF650) samples are 200 °C and 270 °C, respectively, which are lower than those of the other samples (Table 3(a) and 3(b)).

Some publications have shown that the T_{50} and T_{100} of oxide catalysts are different depending on the fabrication method, as shown in Table 4. In some cases, if the single CeO_2 or Fe_2O_3 oxide is used as a catalyst, the T_{50} and T_{100} also decrease quite low [22, 53], but the rest is very high

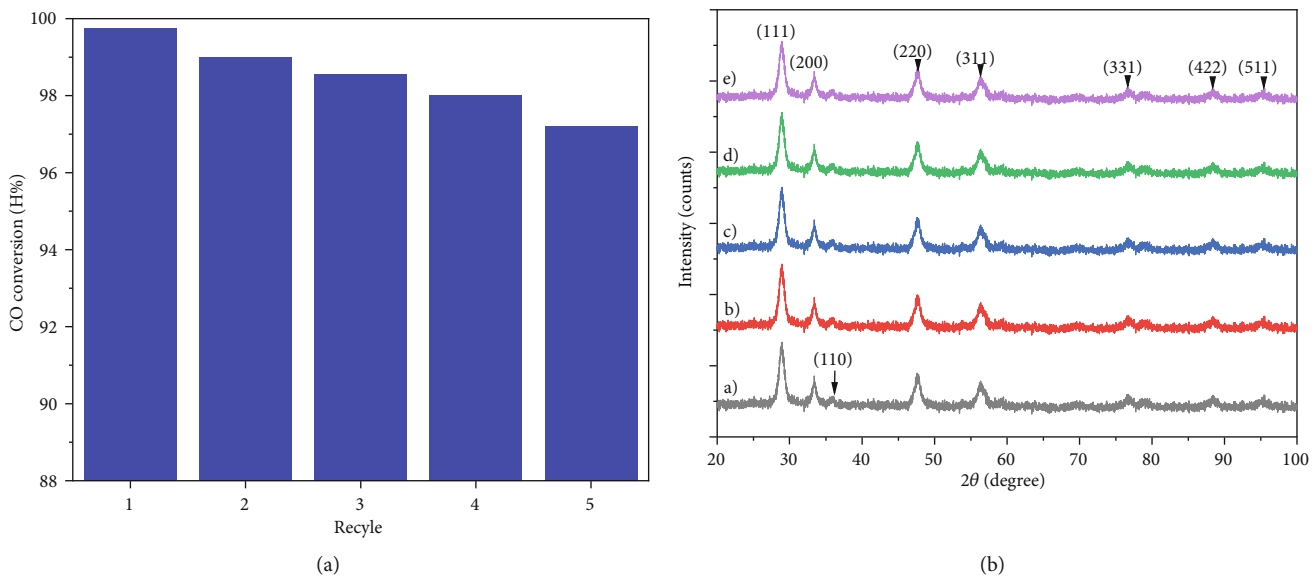

Figure 10: CO conversion of sample CF650(CF11) at T_{100} after 5 recycles (a) and corresponding XRD patterns (A) 1st, (B) 2nd, (C) 3rd, (D) 4th, and (E) 5th (b).

[23, 41, 46, 52, 54–56]. For CeO_2-Fe_2O_3 catalyst materials, several studies have achieved immediate maximum CO conversion (M) at room temperature but are not capable of 100% CO conversion [25]. Some results are quite similar [19, 27, 40], but the others are very high [23, 24, 31, 41].

The correlation between T_{50} and T_{100} temperatures of the CeO_2-Fe_2O_3 mixed oxides is shown in Figure 9. It is seen that the T_{50} and T_{100} are quite low for all samples and the conversion ability is the best corresponding to the CF11 sample calcined at 650°C for 2 h.

Figure 10 shows five oxidation cycles at T_{100} that were used to study the structural and mixed catalytic stability of sample CF11(650). After 5 oxidation cycles, the CO conversion efficiency was lowered to 97.18% (Figure 10(a)). This reduction in CO oxidation performance might be attributed to phase separation in the mixed oxide, as evidenced by the presence of the Fe2O3 phase at peak (110) (Figure 10(b)).

The studied results showed that Fe^{3+} ions joined in CeO_2 crystal lattice, which has caused the deformation of the lattice structure, increasing the quantity of V_O vacancies. The V_O vacancies acted as the reaction centers, thereby promoting easier oxidation processes. The CeO_2-Fe_2O_3 mixed oxide catalysts are fabricated by the combustion method using gel-created TA matter for CO conversion is effective.

4. Conclusion

CeO_2-Fe_2O_3 mixed oxides have been prepared successfully by the combustion method using gel-created tartaric acid. The solid solution of CeO_2-Fe_2O_3 mixed oxides formed a molar ratio of Ce^{+3} ions to Fe^{3+} ions of 1 : 1 at 650 °C for 2 h with a uniform average crystal size of 70 nm and a surface area of 20.22 $m^2.g^{-1}$. In particular, the transformation of metal-ion states in Fe^{3+}/Fe^{2+} and Ce^{4+}/Ce^{3+} pairs through the redox processes have formed a closed loop of Fe-ion oxidation states: $Fe_2O_3 \rightarrow Fe_3O_4 \rightarrow FeO \rightarrow Fe_2O_3$, and maintains the catalytic properties of the CeO_2-Fe_2O_3 mixed oxides. The participation of Fe-metal ions in CeO_2-Fe_2O_3 mixed oxide solution enhanced the density of V_O vacancies and promoted the catalytic reactions of CO conversion. The choice of Ce^{3+} to Fe^{3+} molar ratio of 1 : 1 has halved the needed Ce content. The complete conversion of CO into CO_2 has taken place at a low temperature of 270 °C under deficient O_2 conditions. The studied results can open a prospect of using CeO_2-Fe_2O_3 mixed oxide catalysts for simple CO emission incinerators.

Data Availability

The data used to support the findings of this study are available from the corresponding author upon request.

Conflicts of Interest

The authors declare that they have no conflicts of interest.

Acknowledgments

This research is funded by the Vietnam Academy of Science and Technology (reference number TĐVLTT.01/21-23).

References

[1] C. Mattiuzzi and G. Lippi, "Worldwide epidemiology of carbon monoxide poisoning," *Human & Experimental Toxicology*, vol. 39, no. 4, pp. 387–392, 2020.

[2] H. Kinoshita, H. Türkan, S. Vucinic et al., "Carbon monoxide poisoning," *Toxicology Reports*, vol. 7, pp. 169–173, 2020.

[3] S. R. Eilenberg, K. R. Bilsback, M. Johnson et al., "Field measurements of solid-fuel cookstove emissions from uncontrolled cooking in China, Honduras, Uganda, and India," *Atmospheric Environment*, vol. 190, pp. 116–125, 2018.

[4] Y. Zhang, Q. Li, A. Meng, and C. Chen, "Carbon monoxide formation and emissions during waste incineration in a grate–circulating fluidized bed incinerator," *Waste Management & Research*, vol. 29, no. 3, pp. 294–308, 2011.

[5] M. Xiu, S. Stevanovic, M. M. Rahman, A. M. Pourkhesalian, L. Morawska, and P. K. Thai, "Emissions of particulate matter, carbon monoxide and nitrogen oxides from the residential burning of waste paper briquettes and other fuels," *Environmental Research*, vol. 167, pp. 536–543, 2018.

[6] M. A. Richard, S. L. Soled, R. A. Fiato, and B. A. DeRites, "The behavior of iron oxides in reducing atmospheres," *Materials Research Bulletin*, vol. 18, no. 7, pp. 829–833, 1983.

[7] J. Vansant and P. W. Koziel, "Technical and industrial applications of CO2," in *An Economy Based on Carbon Dioxide and Water*, M. Aresta, I. Karimi, and S. Kawi, Eds., pp. 73–103, Springer, Cham, 2019.

[8] F. Gao, S. Wang, W. Wang, J. Duan, J. Dong, and G. Chen, "Adsorption separation of CO from syngas with CuCl@AC adsorbent by a VPSA process," *RSC Advances*, vol. 8, no. 69, pp. 39362–39370, 2018.

[9] J. A. Hogendoorn, W. P. M. van Swaaij, and G. F. Versteeg, "The absorption of carbon monoxide in COSORB solutions: absorption rate and capacity," *The Chemical Engineering Journal*, vol. 59, no. 3, pp. 243–252, 1995.

[10] C. Xue, W. Hao, W. Cheng et al., "CO adsorption performance of CuCl/activated carbon by simultaneous reduction–dispersion of mixed Cu(II) salts," *Materials*, vol. 12, no. 10, article 1605, 2019.

[11] G. B. Della Mea, L. P. Matte, A. S. Thill et al., "Tuning the oxygen vacancy population of cerium oxide (CeO2−x, 0 < x <0.5) nanoparticles," *Applied Surface Science*, vol. 422, pp. 1102–1112, 2017.

[12] S. Scirè and L. Palmisano, *Cerium Oxide (CeO_2): Synthesis, Properties and Applications*, Elsevier B.V, Amsterdam, Netherlands, firt ed edition, 2020.

[13] C. Maria Magdalane, K. Kaviyarasu, N. Matinise et al., "Evaluation on La_2O_3 garlanded ceria heterostructured binary metal oxide nanoplates for UV/ visible light induced removal of organic dye from urban wastewater," *South African Journal of Chemical Engineering*, vol. 26, pp. 49–60, 2018.

[14] L. He, G. Wang, F. Zhang, Y. Cai, Y. Wang, and I. Djerdj, "Surfactant-assisted synthesis of CeO2 nanoparticles and their application in wastewater treatment," *RSC Advances*, vol. 2, no. 32, pp. 12413–12423, 2012.

[15] N. Sabari Arul, D. Mangalaraj, R. Ramachandran, A. Nirmala Grace, and J. In Han, "Fabrication of CeO2/Fe2O3 composite nanospindles for enhanced visible light driven photocatalyst and supercapacitor electrode," *Journal of Materials Chemistry A*, vol. 3, no. 29, pp. 15248–15258, 2015.

[16] S. Tambat, S. Umale, and S. Sontakke, "Photocatalytic degradation of milling yellow dye using sol–gel synthesized CeO2," *Materials Research Bulletin.*, vol. 76, pp. 466–472, 2016.

[17] M. Kovacevic, B. L. Mojet, J. G. van Ommen, and L. Lefferts, "Effects of morphology of cerium oxide catalysts for reverse water gas shift reaction," *Catalysis Letters*, vol. 146, no. 4, pp. 770–777, 2016.

[18] A. F. Zedan and A. S. AlJaber, "Combustion synthesis of non-precious CuO-CeO_2 nanocrystalline catalysts with enhanced catalytic activity for methane oxidation," *Materials*, vol. 12, no. 6, p. 878, 2019.

[19] M. Lykaki, S. Stefa, S. A. Carabineiro, P. K. Pandis, V. N. Stathopoulos, and M. Konsolakis, "Facet-dependent reactivity of Fe2O3/CeO2 nanocomposites: effect of ceria morphology on CO oxidation," *Catalysts*, vol. 9, no. 4, article 371, 2019.

[20] K. Song, S. Wang, Q. Sun, and D. Xu, "Study of oxidative dehydrogenation of ethylbenzene with CO2 on supported CeO2-Fe2O3 binary oxides," *Arabian Journal of Chemistry*, vol. 13, no. 10, pp. 7357–7369, 2020.

[21] S. Stefa, M. Lykaki, D. Fragkoulis et al., "Effect of the preparation method on the physicochemical properties and the CO oxidation performance of nanostructured CeO_2/TiO_2 oxides," *PRO*, vol. 8, no. 7, p. 847, 2020.

[22] G. Feng, W. Han, Z. Wang, F. Li, and W. Xue, "Highly reducible nanostructured CeO2 for CO oxidation," *Catalysts*, vol. 8, no. 11, p. 535, 2018.

[23] H. Bao, X. Chen, J. Fang, Z. Jiang, and W. Huang, "Structure-activity relation of Fe2O3–CeO2 composite catalysts in CO oxidation," *Catalysis Letters*, vol. 125, no. 1-2, pp. 160–167, 2008.

[24] P. Sudarsanam, B. Mallesham, D. Naga Durgasri, and B. M. Reddy, "Physicochemical characterization and catalytic CO oxidation performance of nanocrystalline Ce-Fe mixed oxides," *RSC Advances*, vol. 4, no. 22, pp. 11322–11330, 2014.

[25] Y. Luo, R. Chen, W. Peng, G. Tang, and X. Gao, "Inverse CeO_2![single bond](https://sdfestaticassets-us- east-1.sciencedirectassets.com/shared- assets/55/entities/sbnd.gif)Fe_2O_3 catalyst for superior low-temperature CO conversion efficiency," *Applied Surface Science*, vol. 416, no. C, pp. 911–917, 2017.

[26] A. A. Ansari, "Optical and structural properties of sol–gel derived nanostructured CeO2 film," *Journal of Semiconductors*, vol. 31, no. 5, article 053001, 2010.

[27] A. Tavakoli, N. Nasiri, Y. Mortazavi, and A. A. Khodadadi, "Cyclic molecular designed dispersion (CMDD) of Fe_2O_3 on CeO_2 promoted by Au for preferential CO oxidation in hydrogen," *International Journal of Hydrogen Energy*, vol. 45, no. 58, pp. 33598–33611, 2020.

[28] H. Shang, X. Zhang, J. Xu, and Y. Han, "Effects of preparation methods on the activity of CuO/CeO2 catalysts for CO oxidation," *Frontiers of Chemical Science and Engineering*, vol. 11, no. 4, pp. 603–612, 2017.

[29] S. Dey and G. C. Dhal, "Cerium catalysts applications in carbon monoxide oxidations," *Materials Science for Energy Technologies*, vol. 3, pp. 6–24, 2020.

[30] R. A. Vazirov, S. Y. Sokovnin, V. G. Ilves, I. N. Bazhukova, N. Pizurova, and M. V. Kuznetsov, "Physicochemical characterization and antioxidant properties of cerium oxide nanoparticles," *Journal of Physics: Conference Series.*, vol. 1115, no. 3, article 032094, 2018.

[31] D. Li, K. Li, R. Xu et al., "Enhanced CH4 and CO oxidation over $Ce_{1-x}Fe_xO_2$ hybrid catalysts by tuning the lattice distortion and the state of surface iron species," *ACS Applied Materials & Interfaces*, vol. 11, no. 21, pp. 19227–19241, 2019.

[32] A. I. Boronin, E. M. Slavinskaya, A. Figueroba et al., "CO oxidation activity of Pt/CeO_2 catalysts below 0 °C: platinum loading effects," *Applied Catalysis B: Environmental*, vol. 286, article 119931, 2021.

[33] O. A. Stonkus, T. Y. Kardash, E. M. Slavinskaya, V. I. Zaikovskii, and A. I. Boronin, "Thermally induced structural evolution of palladium–ceria catalysts. Implication for CO oxidation," *ChemCatChem*, vol. 11, no. 15, pp. 3505–3521, 2019.

[34] K. M. Saoud and M. S. El-Shall, "Physical and chemical synthesis of Au/CeO2 nanoparticle catalysts for room temperature CO oxidation: a comparative study," *Catalysts*, vol. 10, no. 11, p. 1351, 2020.

[35] L. S. Kibis, D. A. Svintsitskiy, T. Y. Kardash et al., "Interface interactions and CO oxidation activity of Ag/CeO_2 catalysts: a new approach using model catalytic systems," *Applied Catalysis A: General*, vol. 570, pp. 51–61, 2019.

[36] V. V. Galvita, H. Poelman, V. Bliznuk, C. Detavernier, and G. B. Marin, "CeO2-modified Fe2O3 for CO2 utilization via chemical looping," *Industrial and Engineering Chemistry Research*, vol. 52, no. 25, pp. 8416–8426, 2013.

[37] D. H. Taffa, I. Hamm, C. Dunkel, I. Sinev, D. Bahnemann, and M. Wark, "Electrochemical deposition of Fe2O3 in the presence of organic additives: a route to enhanced photoactivity," *RSC Advances*, vol. 5, no. 125, pp. 103512–103522, 2015.

[38] Z. Zhang, H. Dong, S. Wei, and Y. Zhang, "Determination of active site densities and mechanisms for soot combustion with O_2 on Fe-doped CeO_2 mixed oxides," *Journal of Catalysis*, vol. 276, no. 1, pp. 16–23, 2010.

[39] S. W. Hoh, L. Thomas, G. Jones, and D. J. Willock, "A density functional study of oxygen vacancy formation on α-Fe2O3(0001) surface and the effect of supported au nanoparticles," *Research on Chemical Intermediates*, vol. 41, no. 12, pp. 9587–9601, 2015.

[40] O. H. Laguna, M. A. Centeno, G. Arzamendi, L. M. Gandía, F. Romero-Sarria, and J. A. Odriozola, "Iron-modified ceria and Au/ceria catalysts for total and preferential oxidation of CO (TOX and PROX)," *Catalysis Today*, vol. 157, no. 1-4, pp. 155–159, 2010.

[41] T. R. Sahoo, M. Armandi, R. Arletti et al., "Pure and Fe-doped CeO2 nanoparticles obtained by microwave assisted combustion synthesis: physico-chemical properties ruling their catalytic activity towards CO oxidation and soot combustion," *Applied Catalysis B: Environmental*, vol. 211, pp. 31–45, 2017.

[42] S. K. Chawla, K. Prabhjyot, R. K. Mudsainiyan, S. S. Meena, and S. M. Yusuf, "Effect of fuel on the synthesis, structural, and magnetic properties of M-type hexagonal ferrites by sol-gel auto-combustion method," *Journal of Superconductivity and Novel Magnetism*, vol. 28, no. 5, pp. 1589–1599, 2015.

[43] A. A. Ali, I. S. Ahmed, and E. M. Elfky, "Auto-combustion synthesis and characterization of iron oxide nanoparticles (α-Fe2O3) for removal of lead ions from aqueous solution," *Journal of Inorganic and Organometallic Polymers and Materials*, vol. 31, no. 1, pp. 384–396, 2021.

[44] C. A. Strydom and C. P. J. van Vuuren, "The thermal decomposition of cerium(III) nitrate," *Journal of thermal analysis*, vol. 32, no. 1, pp. 157–160, 1987.

[45] A. Lassoued, B. Dkhil, A. Gadri, and S. Ammar, "Control of the shape and size of iron oxide (α-Fe_2O_3) nanoparticles synthesized through the chemical precipitation method," *Results in Physics*, vol. 7, no. 7, pp. 3007–3015, 2017.

[46] M.-N. Guo, C.-X. Guo, L.-Y. Jin, Y.-J. Wang, J.-Q. Lu, and M.-F. Luo, "Nano-sized CeO_2 with extra-high surface area and its activity for CO oxidation," *Materials Letters*, vol. 64, no. 14, pp. 1638–1640, 2010.

[47] I. Moog, C. Feral-Martin, M. Duttine et al., "Local organization of Fe3+ into nano-CeO2 with controlled morphologies and its impact on reducibility properties," *Journal of Materials Chemistry A*, vol. 2, no. 47, pp. 20402–20414, 2014.

[48] D. N. Nhiem, L. M. Dai, N. D. Van, and D. T. Lim, "Catalytic oxidation of carbon monoxide over nanostructured CeO2-Al2O3 prepared by combustion method using polyvinyl alcohol," *Ceramics International*, vol. 39, no. 3, pp. 3381–3385, 2013.

[49] O. Seibert, J. Grégr, and P. Kejzlar, "The preparation of iron oxide nanoparticles by a self-combustion method," *Manufacturing Technology*, vol. 19, no. 4, pp. 680–684, 2019.

[50] R. C. Pullar, R. M. Novais, A. P. Caetano, M. A. Barreiros, S. Abanades, and F. A. C. Oliveira, "A review of solar thermochemical CO2 splitting using ceria-based ceramics with designed morphologies and microstructures," *Frontiers in Chemistry*, vol. 7, article 601, 2019.

[51] R. Brackmann, F. S. Toniolo, and M. Schmal, "Synthesis and characterization of Fe-doped CeO2 for application in the NO selective catalytic reduction by CO," *Topics in Catalysis*, vol. 59, no. 19-20, pp. 1772–1786, 2016.

[52] A. Gupta, A. Kumar, U. V. Waghmare, and M. S. Hegde, "Origin of activation of lattice oxygen and synergistic interaction in bimetal-ionic Ce0.89Fe0.1Pd0.01O2–δCatalyst," *Maternité*, vol. 21, no. 20, pp. 4880–4891, 2009.

[53] J.-L. Cao, Y. Wang, X.-L. Yu, S.-R. Wang, S.-H. Wu, and Z.-Y. Yuan, "Mesoporous CuO–Fe2O3 composite catalysts for low-temperature carbon monoxide oxidation," *Applied Catalysis B: Environmental*, vol. 79, no. 1, pp. 26–34, 2008.

[54] A. Biabani-Ravandi, M. Rezaei, and Z. Fattah, "Catalytic performance of Ag/Fe2O3 for the low temperature oxidation of carbon monoxide," *Chemical Engineering Journal*, vol. 219, pp. 124–130, 2013.

[55] M. Z. Tana, J. Li, H. Li, Y. Li, and W. Shen, "Morphology-dependent redox and catalytic properties of CeO2 nanostructures: nanowires, nanorods and nanoparticles," *Catalysis Today*, vol. 148, no. 1-2, pp. 179–183, 2009.

[56] X. Zhang, F. Hou, Y. Yang et al., "A facile synthesis for cauliflower like CeO2 catalysts from Ce-BTC precursor and their catalytic performance for CO oxidation," *Applied Surface Science*, vol. 423, pp. 771–779, 2017.

[57] C. Ho, J. C. Yu, T. Kwong, A. C. Mak, and S. Lai, "Morphology-controllable synthesis of mesoporous CeO2 nano- and microstructures," *Chemistry of Materials*, vol. 17, no. 17, pp. 4514–4522, 2005.

[58] R. D. Kerkar and A. V. Salker, "Significant effect of multi-doped cerium oxide for carbon monoxide oxidation studies," *Materials Chemistry and Physics*, vol. 253, p. 123326, 2020.